

Bose-Einstein Condensation of Quasi-Particles by Rapid Cooling

Authors: M. Schneider¹, T. Brächer¹, V. Lauer¹, P. Pirro¹, D. A. Bozhko¹, A. A. Serga¹, H. Yu. Musiienko-Shmarova¹, B. Heinz^{1,2}, Q. Wang¹, T. Meyer¹, F. Heussner¹, S. Keller¹, E. Th. Papaioannou¹, B. Lägel³, T. Löber³, V. S. Tiberkevich⁴, A. N. Slavin⁴, C. Dub⁵, B. Hillebrands¹, and A.V. Chumak¹

¹Fachbereich Physik and Landesforschungszentrum OPTIMAS, Technische Universität Kaiserslautern, D-67663 Kaiserslautern, Germany.

²Graduate School Materials Science in Mainz, Staudingerweg 9, D-55128 Mainz, Germany.

³Nano Structuring Center, Technische Universität Kaiserslautern, D-67663 Kaiserslautern, Germany.

⁴Department of Physics, Oakland University, Rochester, MI 48309, USA.

⁵INNOVENT e.V. Technologieentwicklung, Prüssingstraße 27B, D-07745 Jena, Germany.

The fundamental phenomenon of Bose-Einstein Condensation (BEC) has been observed in different systems of real and quasi-particles. The condensation of real particles is achieved through a major reduction in temperature while for quasi-particles a mechanism of external injection of bosons by irradiation is required. Here, we present a novel and universal approach to enable BEC of quasi-particles and to corroborate it experimentally by using magnons as the Bose-particle model system. The critical point to this approach is the introduction of a disequilibrium of magnons with the phonon bath. After heating to an elevated temperature, a sudden decrease in the temperature of the phonons, which is approximately instant on the time scales of the magnon system, results in a large excess of incoherent magnons. The consequent spectral redistribution of these magnons triggers the Bose-Einstein condensation.

Bosons are particles of integer spin that allow for the fundamental quantum effect of Bose-Einstein Condensation (BEC), which manifests itself in the formation of a macroscopic coherent state in an otherwise incoherent, thermalized many-particle system. The phenomenon of BEC was originally predicted for an ideal gas by Albert Einstein in 1924 based on the theory developed by Satyendra Nath Bose. Nowadays, Bose-Einstein condensates are investigated experimentally in a variety of different systems which includes real particles such as ultra-cold gases (1, 2) as well as quasi-particles with the likes of exciton-polaritons (3, 4), photons (5, 6) or magnons (7-9). The phenomenon can be reached by a major decrease in the system temperature or by an increase in the particle density. In order to condensate atomic gases, extremely low temperatures on the order of mK are required since the density of such gases must be very low to prevent their cohesion. In contrast, the quasi-stationary cooling of a quasi-particle system is accompanied by a decrease in its population and prevents BEC. Thus, an artificial injection of bosons is required to reach the threshold for BEC. Since quasi-particle systems allow for high

densities of bosons, BEC by quasi-particle injection is possible even at room temperature. Prominent examples are the injection of exciton-polaritons by a laser (3-6) or of magnons by microwave parametric pumping (8-10).

In this letter, we propose and demonstrate experimentally a different and universal way to achieve BEC of quasi-particles. In a solid body, each quasi-particle system interacts with the phonon bath and these two systems stay in equilibrium in a quasi-stationary state. An instant reduction in the phonon temperature results in a large excess of quasi-particles when compared to the equilibrium state at the new temperature. This kind of injection is a-priori incoherent and injects bosons over the entire energy spectrum. The consequent redistribution of the quasi-particles due to the multi-particle and particle-phonon scattering processes results in an increase in the chemical potential μ required for the BEC.

The energy-distribution $n(hf, \mu, T)$ of the density of bosons depends on temperature T and is described by the Bose-Einstein distribution function multiplied with their energy-dependent density of states $D(hf)$:

$$n(hf, \mu(t), T(t)) = \frac{D(hf)}{\exp\left(\frac{hf - \mu(t)}{k_B T(t)}\right) - 1}, \quad (1)$$

where hf is the energy of the quasi-particle, f is its frequency, t is the elapsed time, $T(t)$ is the phonon or lattice temperature, $\mu(t)$ is the chemical potential, h is Planck's constant, and k_B is Boltzmann's constant. In the work presented, BEC is studied experimentally using a magnon system. For their description, the approximated density of states for ferromagnetic exchange magnons is used: $D(hf) \propto \sqrt{f - f_{\min}}$, where f_{\min} is the frequency at the bottom of the magnon spectrum. The dashed blue lines in all panels of Fig. 1B show the steady-state density distributions when the magnon and the phonon systems are in equilibrium at room temperature $T = T_{\text{Room}}$ for $\mu = 0$. In order to achieve a BEC of quasi-particles the chemical potential μ has to be increased up to the value of the minimum magnon energy hf_{\min} . In this case, Equation (1) diverges, reflecting the condensation of the quasi particles into the same quantum state at the smallest energy of the system. The distribution of magnon density in the particular case of $\mu = hf_{\min}$ at room temperature $T = T_{\text{Room}}$ is shown in Fig. 1B by the dashed green lines.

Our approach to provide conditions for the BEC is as follows. First, the temperature of the phonon system is raised to a certain critical value. This rise in temperature increases the number of phonons and magnons simultaneously (see point "1" in Fig. 1A). The magnon density in the heated quasi-equilibrium state is given by Eq. 1 at the increased temperature and $\mu = 0$ is depicted in the Panel "1" in Fig. 1B by the solid red line. The proposed mechanism for BEC formation is based on the rapid cooling of the phonon system as it is shown in Fig. 1A. As the lattice temperature drops, the distribution of magnons changes rapidly. The consequent magnon distribution (see Panel "2" in Fig. 1B) is calculated following the dynamic rate equations given in the Supplementary Materials. Two mechanisms are of highest importance for this magnon redistribution. The first one is the phonon-magnon coupling that transfers energy from the magnon to the phonon system. With the assumption of the simplest case of viscous Gilbert damping (11), the rate of decay of the magnons is proportional to their energy. At the same time, magnon-magnon scattering processes (11), i.e., the weak interactions within the magnon system, allow for a redistribution of magnons towards low energies. For simplicity, our model only

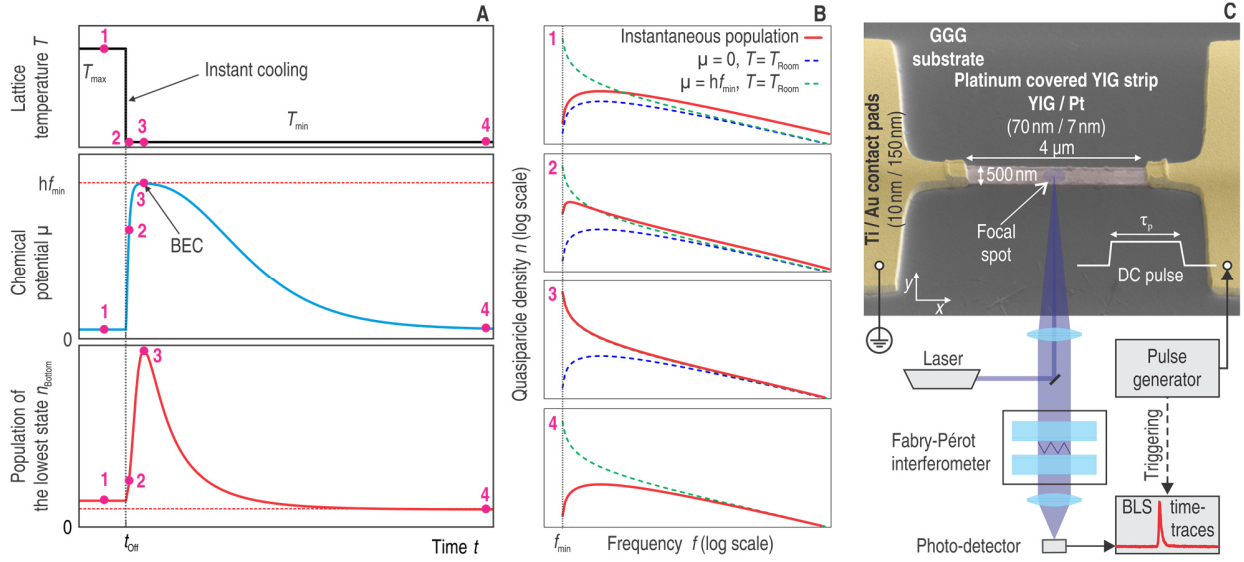


Figure 1. A) and B) show schematic depiction of the condensation process. A) shows the time evolution of the temperature of the phonon system (top panel), the quasi-particle chemical potential (middle panel) and the quasi-particle population at the lowest energy state (bottom panel). The time of the instant cooling is marked by t_{off} . B) shows the quasi-particle density as a function of frequency. The red lines in the different panels show the densities for the different times marked in Fig. 1A. Dashed blue lines: Steady-state room-temperature distributions. Dashed green lines: Room-temperature distribution with $\mu = hf_{\text{min}}$. C) Structure under investigation and sketch of the experimental setup.

considers the case of quasi-particle conserving four magnon processes (see Supplementary Materials) but, other mechanism like three-magnon scattering and Cherenkov radiation will also contribute to the same process (11, 12). Consequently, the density of low-energy magnons increases while the high-energy magnons dissipate. This results in an increase in the chemical potential μ of magnons over time – see middle panel in Fig. 1A. If the critical number of magnons in the heated state is reached, the chemical potential will rise up to the minimum magnon energy hf_{min} (see Panel “3” in Fig. 1B) and BEC of magnons occurs. This is manifested in the form of a sharp increase in the magnon density at the lowest energy state shown in the bottom panel of Fig. 1A. Ultimately, the magnon system returns to room-temperature equilibrium (see point “4” in Figs. 1A and 1B) due to scattering into the phonon system, which is responsible for the finite magnon lifetime.

The proposed mechanism can be used universally for all bosonic quasi-particles showing internal inelastic scattering mechanisms and that are interacting with the phonon system. The key experimental challenge, which has inhibited its realization so far, is the achievement of a sufficiently high cooling rate. Recent progress in the creation of (magnetic) nano-structures enabled quasi-instant cooling. In these structures, the heat diffusion from a heated nano-structure to the quasi-bulk surroundings ensures a cooling time shorter than the characteristic magnon scattering time and the characteristic interaction time of the quasi-particles with the phonon bath.

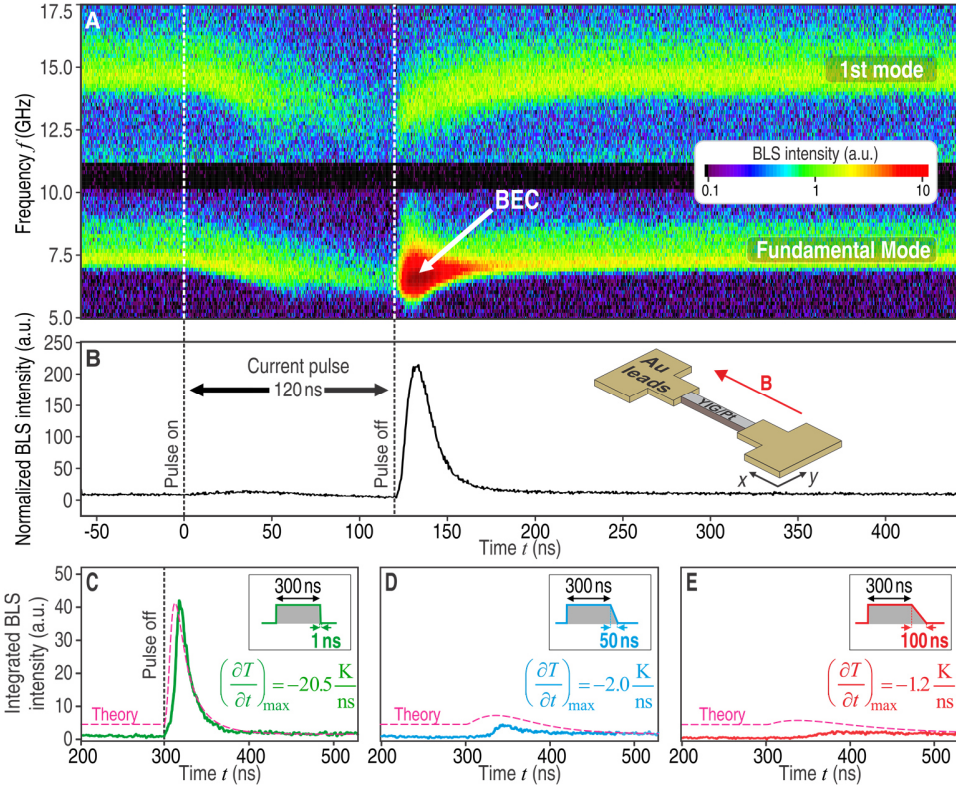


Figure 2. A) Depicts the BLS spectrum as a function of time. The BLS signal (color-coded, log scale) is proportional to the density of magnons. The vertical dashed lines indicate the start and end of the pulse. Switching off the pulse results in the formation of a pronounced magnon signal at the bottom of the magnon band. B) Normalized magnon intensity integrated from 4.95 GHz to 8.1 GHz as a function of time ($\mathbf{B} \parallel \mathbf{x}$). The BEC of magnons is clearly visible. The inset shows the sample geometry and the coordinate system used. C) The magnon intensity at the bottom of the spectrum (analogue to panel B but with $\tau_p = 300$ ns and $\mathbf{B} \parallel \mathbf{y}$). The pink dashed line shows the magnon density at the bottom of the spectrum calculated using the dynamic rate equations discussed in the Supplement with $\tau_{\text{Fall}} = 1$ ns. D) The same experiment with artificially increased fall times of 50 ns (blue line). Here, the BEC is strongly suppressed. The pink dashed line shows the calculated magnon density for $\tau_{\text{Fall}} = 50$ ns. For this slow cooling, the chemical potential reaches a maximal value of only $0.58 \times h f_{\text{min}}$. E) The same experiment with artificially increased fall times of 100 ns (red line) and theory for $\tau_{\text{Fall}} = 100$ ns (pink line). See the inset for the time profiles of the pulses.

In our study, of a model system, we investigate magnons at room temperature in an Yttrium Iron Garnet (YIG) (13) – Platinum nano-strip (width 500 nm, length 5 μ m, YIG thickness 70 nm, Pt thickness 7 nm (see Fig. 1C). A biasing magnetic field sufficiently large to magnetize the strip along the field direction is applied either in-plane parallel ($\mathbf{B} \parallel \mathbf{x}$) or perpendicular ($\mathbf{B} \parallel \mathbf{y}$) to the long axis of the strip – for the exact geometry, see Fig. 1C. Ti/Au leads have been deposited on top of the strip to apply electric current pulses to the Pt overlayer,

which heat up the YIG/Pt structure due to Joule heating. Switching off the pulse results in a fast cooling with rates on the order of tens of Kelvin per nanosecond. This fast cooling is provided by the heat diffusion to the quasi-bulk Gadolinium Gallium Garnet (GGG) substrate and to the Ti/Au leads. In order to measure the time evolution of the magnon density in the YIG strip, micro-focused time-resolved Brillouin Light Scattering (BLS) spectroscopy (14) is used (see Supplementary Materials).

Figure 2A shows the measured magnon spectrum as a function of time when the voltage pulse with a duration of $\tau_p = 120$ ns and a rise and fall time of $\tau_{\text{Rise}} = \tau_{\text{Fall}} = 1$ ns is applied. The beginning and the end of the applied pulse are indicated by the vertical dashed lines. The amplitude of the voltage pulse was $U = 0.9$ V, corresponding to an estimated current density of 7.8×10^{11} A/m² in the Pt overlayer. The thermal population of two magnon modes is visible before the current pulse is applied. The magnon mode at $f_F = 7.8$ GHz has the smallest frequency and is the fundamental mode. The magnon mode of frequency $f_{\text{1st mode}} = 15.1$ GHz is the first standing thickness mode (11). Once the current pulse is switched on at the time $t = 0$ ns, the frequencies of both modes decrease with time due to heating and the consequent decrease in the saturation magnetization M_s and the exchange stiffness D_{ex} of YIG (15). Another observable effect is the decrease of the BLS intensity during the current pulse that is due to a temperature-dependent decrease in the sensitivity of the BLS (16).

One can clearly see in Fig. 2A that switching off the current pulse at time $t = \tau_p$ results in the formation of a pronounced magnon signal at the frequency of the fundamental mode which corresponds to the bottom of the magnon spectrum. This is the characteristic fingerprint of the process of BEC of magnons described by the proposed theoretical model. The signal maximum is reached approximately 10 ns after the current pulse is switched off. Afterwards, the BLS intensity decreases exponentially, corresponding to a magnon lifetime of 21 ± 4 ns. In addition, the recovery of the frequency of both modes is observed. The black line in Fig. 2B presents the time evolution of the BLS intensity integrated over the frequency range at the bottom of the magnon spectrum. A clear agreement with the result of the simplified theoretical model in the bottom panel of Fig. 1A is visible. In addition, the same experiment was performed when the field was applied perpendicular to the long axis of the strip ($\mathbf{B} \parallel \mathbf{y}$, see Supplementary Materials). No qualitative difference between the results was observed excluding a Spin Hall Effect induced Spin Transfer Torque (17,18) as the responsible mechanism for the phenomenon. In addition, the temperature gradient and the corresponding Spin Seebeck effect (19-21) cannot explain our experimental observation since the gradient is formed quasi-instantaneously after the current pulse is switched on and vanishes immediately as it is switched off. The BEC, as opposite, takes place a few nanoseconds after the pulse was switched off at times at which the gradient has already disappeared.

To verify the crucial role of the fast cooling for the BEC, additional measurements were performed in which the current pulses were switched off with longer fall times of 50 ns and 100 ns. For these measurements, the pulse duration was increased to $\tau_p = 300$ ns. As can be seen from Fig. 2C, the increased pulse duration does not inhibit the BEC formation. The influence of the fall time is shown in Fig. 2D,E. It is evident that the condensate disappears for long fall times, i.e, slow cooling rates. The maximal temperature approaches a value of $T_{\text{sim}}^{\text{max}} = 491$ K at the end of the current pulse according to simulations performed with COMSOL Multiphysics

(see Supplementary Materials). The maximal cooling rates of the phonon system $(\partial T / \partial t)_{\max}$ obtained from these simulations are also indicated in the Figures. The values clearly demonstrate that the cooling rate of 2 K/ns is already too slow to trigger the magnon BEC, while a rate of 20.5 K/ns is still fast enough. Moreover, the simulations show that the cooling rate is not constant and decreases with time. In order to model this, the simple approach of an exponential decay $T \propto \exp(-t/\tau_{\text{Fall}})$ of the temperature was used in the theoretical model instead of the step function discussed in Fig. 1. The theoretical results are presented in Fig. 2C-E and support the experimental findings – the BEC is observed only in the first case of $\tau_{\text{Fall}} = 1$ ns.

The BEC of quasi-particles is a threshold-like phenomenon that takes place when the chemical potential μ reaches the minimal energy level hf_{\min} . This implies, that in this experiment, a certain threshold temperature needs to be exceeded which corresponds to a certain critical magnon density in the system. Therefore, for a given pulse duration τ_p , a certain voltage needs to be applied to reach this critical density. The clear threshold-like behaviour is visible in Fig. 3A, in which the frequency-integrated BLS intensity (color-coded) is plotted as a function of time and voltage for $\tau_p = 40$ ns. The extracted maximum magnon intensity is depicted in Fig. 3B as a function of the applied voltage. It can be clearly seen that the application of voltage pulses with amplitudes smaller than ± 1.2 V does not result in BEC, since the critical magnon density is not reached. The threshold magnon density is exceeded and the magnon condensate is formed only for larger voltages.

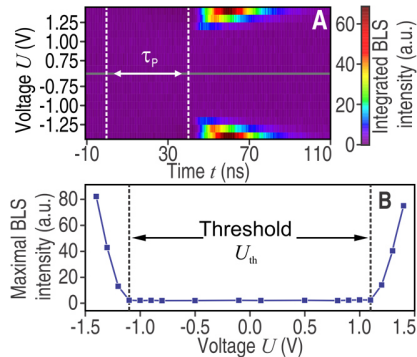


Figure 3. A) Measured intensity of magnons at the bottom of the spectrum (color-coded) as a function of time and applied voltage ($\mathbf{B}||\mathbf{y}$). The applied current pulse is marked by the vertical dashed lines. B) Maximal magnon intensity as a function of the applied voltage extracted from A. A clear threshold is visible at 1.2 V, independent of the current polarity.

In conclusion, a novel way to create a magnon Bose-Einstein condensate by rapid cooling in an individual magnetic nano-structure has been proposed and verified experimentally. BEC of magnons has been achieved in a typical spintronic structure by the application of current pulses with powers of a few mW rather than by the usage of (intricate) high-power microwave pumping. This paves the way for the usage of macroscopic quantum magnon states in conventional spintronics and to on-chip solid-state quantum computing. We would like to stress that the observed way to BEC is genuine to any solid-state quasi-particles in exchange with the phonon bath. The injection mechanism is originally incoherent which is in direct opposition to laser or microwave irradiation, and can be applied to other bosonic systems such as exciton-polaritons and photons in cavities.

References:

1. M. H. Anderson, J. R. Ensher, M. R. Matthews, C. E. Wieman, E. A. Cornell, Observation of Bose–Einstein condensation in a dilute atomic vapor. *Science* **269**, 198–201 (1995).
2. B. Santra, C. Baals, R. Labouvie, A. B. Bhattacherjee, A. Pelster, H. Ott, Measuring finite-range phase coherence in an optical lattice using Talbot interferometry. *Nat. Commun.* **8**, 15601 (2017).
3. J. Kasprzak, M. Richard, S. Kundermann, A. Baas, P. Jeambrun, J. M. J. Keeling, F. M. Marchetti, M. H. Szymańska, R. André, J. L. Staehli, V. Savona, P. B. Littlewood, B. Deveaud, L. Si Dang, Bose–Einstein condensation of exciton polaritons. *Nature* **443**, 409–414 (2006).
4. G. Lerario, A. Fieramosca, F. Barachati, D. Ballarini, K. S. Daskalakis, L. Dominici, M. De Giorgi, S. A. Maier, G. Gigli, S. Kéna-Cohen, D. Sanvitto, Room-temperature superfluidity in a polariton condensate. *Nat. Phys.* **13**, 837–841 (2017).
5. J. Klaers, J. Schmitt, F. Vewinger, M. Weitz, Bose–Einstein condensation of photons in an optical microcavity. *Nature* **468**, 545–548 (2010).
6. T. Damm, J. Schmitt, Q. Liang, D. Dung, F. Vewinger, M. Weitz, J. Klaers, Calorimetry of a Bose–Einstein-condensed photon gas. *Nat. Commun.* **7**, 11340 (2016).
7. T. Nikuni, M. Oshikawa, A. Oosawa, H. Tanaka, Bose–Einstein condensation of dilute magnons in $TiCuCl_3$. *Phys. Rev. Lett.* **84**, 5868–5871 (2000).
8. S. O. Demokritov, V. E. Demidov, O. Dzyapko, G. A. Melkov, A. A. Serga, B. Hillebrands, A.N. Slavin, Bose–Einstein condensation of quasi-equilibrium magnons at room temperature under pumping. *Nature* **443**, 430–433 (2006).
9. A. A. Serga, V. S. Tiberkevich, C. W. Sandweg, V. I. Vasyuchka, D. A. Bozhko, A. V. Chumak, T. Neumann, B. Obry, G. A. Melkov, A. N. Slavin, B. Hillebrands, Bose–Einstein condensation in an ultra-hot gas of pumped magnons. *Nat. Commun.* **5**, 3452 (2014).
10. T. Brächer, P. Pirro, B. Hillebrands, Parallel pumping for magnon spintronics: Amplification and manipulation of magnon spin currents on the micron-scale. *Phys. Rep.* **699**, 1–34 (2017).
11. A. G. Gurevich, G. A. Melkov, *Magnetization oscillations and waves* (CRC, 1996).
12. J. Hüser “Kinetic theory of magnon Bose-Einstein condensation”, PhD thesis, Westfälische Wilhelms-Universität Münster, Münster, Germany (2016).
13. C. Dubs, O. Surzhenko, R. Linke, A. Danilewsky, U. Brückner, J. Dellith, Sub-micrometer yttrium iron garnet LPE films with low ferromagnetic resonance losses. *J. Phys. D: Appl. Phys.* **50**, 204005 (2017).
14. T. Sebastian, K. Schultheiss, B. Obry, B. Hillebrands, H. Schultheiss, Micro-focused Brillouin light scattering: imaging spin waves at the nanoscale. *Front. Phys.* **3**, 35 (2015).
15. V. Cherepanov, I. Kolokolov, V. L'vov, The saga of YIG. *Phys. Rep.* **229**, 81–144 (1993).
16. K. S. Olsson, K. An, X. Ma, S. Sullivan, V. Venu, M. Tsoi, J. Zhou, L. Shi, X. Li, Temperature-dependent Brillouin light scattering spectra of magnons in yttrium iron garnet and permalloy. *Phys. Rev. B* **96**, 024448 (2017).
17. A. V. Chumak, V. I. Vasyuchka, A. A. Serga, B. Hillebrands, Magnon spintronics. *Nat. Phys.* **11**, 453 (2015).

18. V. E. Demidov, S. Urazhdin, G. de Loubens, O. Klein, V. Cros, A. Anane, S. O. Demokritov, Magnetization oscillations and waves driven by pure spin currents. *Phys. Rep.* **673**, 1 (2017).
19. G. E. W. Bauer, E. Saitoh, B. J. van Wees, Spin caloritronics. *Nature Mater.* **11**, 391–399 (2012).
20. S. A. Bender, Y. Tserkovnyak, Thermally driven spin torques in layered magnetic insulators. *Phys. Rev. B* **93**, 064418 (2016).
21. C. Safranski, I. Barsukov, H. K. Lee, T. Schneider, A. A. Jara, A. Smith, H. Chang, K. Lenz, J. Lindner, Y. Tserkovnyak, M. Wu, I. N. Krivorotov, Spin caloritronic nano-oscillator. *Nat. Commun.* **8**, 117 (2017).

Acknowledgements:

This research has been supported by ERC Starting Grant 678309 MagnonCircuits, ERC Advanced Grant 694709 Super-Magnonics, by the DFG in the framework of the Research Unit TRR 173 “Spin+X” (Projects B01 and B07) and Project DU 1427/2-1, by the grants Nos. EFMA-1641989 and ECCS-1708982 from the National Science Foundation of the USA, and by the DARPA M3IC grant under the contract W911-17-C-0031.

Supplementary Materials

to the manuscript “**Bose-Einstein Condensation of Quasi-Particles by Rapid Cooling**” by M. Schneider, T. Brächer, V. Lauer, P. Pirro, D. A. Bozhko, A. A. Serga, H. Yu. Musiienko-Shmarova, B. Heinz, Q. Wang, T. Meyer, F. Heussner, S. Keller, E. Th. Papaioannou, B. Lägel, T. Löber, V. S. Tiberkevich, A. N. Slavin, C. Dubs, B. Hillebrands, and A. V. Chumak.

Content of the Supplementary Materials

1. Theoretical model of the magnon thermalization process	1
2. Fabrication of the YIG/Pt nano-structures under investigation	5
3. Spin-wave dispersion in the YIG nano-structures	5
4. Measurements of the magnon density by time-resolved Brillouin Light Scattering (BLS) spectroscopy	7
5. Simulations of the temporal evolution within the YIG/Pt nano-structure by COMSOL Multiphysics Software	7
6. Dependence of the BEC on the parameters of the experiment and on the direction of the applied magnetic field	11
7. Dependence of the BEC threshold on the current pulse duration	13

1. Theoretical model of the magnon thermalization process

The thermalization of a magnon gas in response to rapid changes of the lattice temperature can be modelled by the following model. For simplicity, we assume that the magnon distribution remains isotropic and depends only on the magnon frequency f , i.e. it is described by the distribution function $n(f, t)$. In the quasi-equilibrium state with lattice temperature $T_L(t)$ and chemical potential $\mu(t)$, the distribution function can be presented in the usual Bose-Einstein form¹,

$$n(hf, t) = n_{\text{eq}}(f, T_L(t), \mu(t)) = \frac{1}{\exp\left(\frac{hf - \mu(t)}{k_B T_L(t)}\right) - 1}, \quad (2)$$

where k_B is Boltzmann’s constant and h is Plank’s constant.

Numerical calculations were performed on a uniform frequency grid:

¹ L. Pitaevski, S. Stringari, *Bose Einstein Condensation* (Clarendon, Oxford, 2003).

$$f_k = f_{\min} + \Delta f k, \quad (3)$$

where k is the step number and Δf is the grid cell size.

Now, instead of the continuous distribution function $n(f, t)$ we obtain a discrete set of magnon population numbers:

$$n_k(t) = n(f_k, t).$$

The dynamics of the population numbers $n_k(t)$ can be described by the following set of equations:

$$D_k \left[\frac{dn_k}{dt} + \Gamma_k (n_k - n_k^0(t)) \right] = N_k, \quad (4)$$

where $D_k = D(f_k)$ is the density of states for the k -th magnon level ($D_k n_k$ is the density of magnons in the frequency range $f_k \pm \Delta f/2$). The density of states is determined by the dispersion law of quasi-particles and the dimensionality of space. In our case, for a quadratic dispersion in the 3D case²:

$$D_k(f_k) = \Delta f \sqrt{f_k - f_{\min}} \quad (5)$$

For the lowest state $k = 0$, $D_0 = 1/V$ was taken, where V is the sample's volume.

$\Gamma_k = \Gamma(f_k)$ in Eq. (4) is the spin-lattice relaxation time, for which one can use the simple “Gilbert” approximation of viscous damping³

$$\Gamma(f) = \alpha_G f. \quad (6)$$

$n_k^0(t) = n_0(f_k, t)$ in Eq. (4) is the instantaneous equilibrium magnon population, which is determined by the instantaneous lattice temperature $T_L(t)$

$$n^0(f, t) = n_{\text{eq}}(f, T_L(t), \mu = 0). \quad (7)$$

The right-hand side of Eq. (4) N_k describes magnon transitions due to nonlinear four-magnon processes (11). We consider the simplest model of nonlinear magnon scattering, in which only the scattering of magnons with similar energies was taken into account. Namely, we considered only the scattering processes of the form

$$f_k + f_k \leftrightarrow f_{k+1} + f_{k-1}. \quad (8)$$

The net rate of such processes is

$$F_k = C_k \left[n_k^2 (n_{k+1} + 1)(n_{k-1} + 1) - n_{k+1} n_{k-1} (n_k + 1)^2 \right], \quad (9)$$

where $C_k = C \sqrt{f_k - f_{\min}} \left(\frac{f_k - f_{\min}}{\Delta f} \right)^3$. Here the constant C is a fitting parameter, which defines the efficiency of the four magnon scattering processes.

² C. Kittel, Introduction to Solid State Physics, (Wiley, 2005).

³ D. D. Stancil and A. Prabhakar, Spin Waves: Theory and applications (Springer, 2009).

The four magnon term N_k in Eq. (4) has the form

$$N_k = F_{k+1} - 2F_k + F_{k-1}. \quad (10)$$

This constitutes a closed system of equations for the determination of the dynamics of $n_k(t)$ for a given lattice temperature temporal profile $T_L(t)$.

The dynamics of the magnon population number $n_k(t)$ is obtained by solving Eq. (4) numerically with the parameters shown in Table S1.

The results of these numerical calculations are shown in Fig. S2. The lattice temperature temporal profile $T_L(t)$ is assumed to be a step-like function, which changes from an elevated temperature T_1 to room temperature T_0 in the moment of time $t_{\text{Off}}=0$ as is shown in the upper panel in Fig. S2A. The simulated magnon densities $D_{knk}(t)$ are exemplarily plotted for four characteristic times in Fig. S2B. The calculated magnon distributions $n_k(t)$, are fitted with the Bose-Einstein distribution function in order to obtain the corresponding chemical potential $\mu(t)$. The procedure of this fitting is as follows. First, we linearize the Bose-Einstein distribution:

$$\ln\left(\frac{1}{n(f,t)}+1\right) = \frac{hf}{k_B T_{\text{eff}}(t)} - \frac{\mu(t)}{k_B T_{\text{eff}}(t)}. \quad (11)$$

Parameter	Value	
Width of the strip	500 nm	1000 nm
Current pulse duration τ_P	120 ns	300 ns
Applied voltage U	0.9 V	1.05 V
Room temperature T_0	288 K	288 K
Elevated temperature T_1	431.4 K	491 K
Gilbert damping constant α_G	1.5×10^{-3}	1.5×10^{-3}
Maximal frequency f_{max}	600 GHz	600 GHz
Frequency step Δf	250 MHz	250 MHz
Four-magnon scattering efficiency C	0.07	0.004

Table S1. Parameters used for the calculations of the magnon density according to the developed quasi-analytical theoretical model for two different experimentally investigated strips.

Consequently, the right-hand-side of Eq. (11) is a linear function of energy (frequency). We fit the low-energy area (below 50 GHz) of the magnon distribution. The fit converges at every time point, indicating that the low-energy magnons are in equilibrium at every instance of time. From fitting the simulated distributions at each moment of time, we obtain the time

dependence of the chemical potential $\mu(t)$. The resulting dependence is shown in the middle panel in Fig. S2A. In order to compare to the experimental data (see Fig. 2 in the main manuscript), we performed an integration of the magnon density $D_{knk}(t)$ over the same frequency range as in the experiment. The corresponding plot is shown in Fig. S2A.

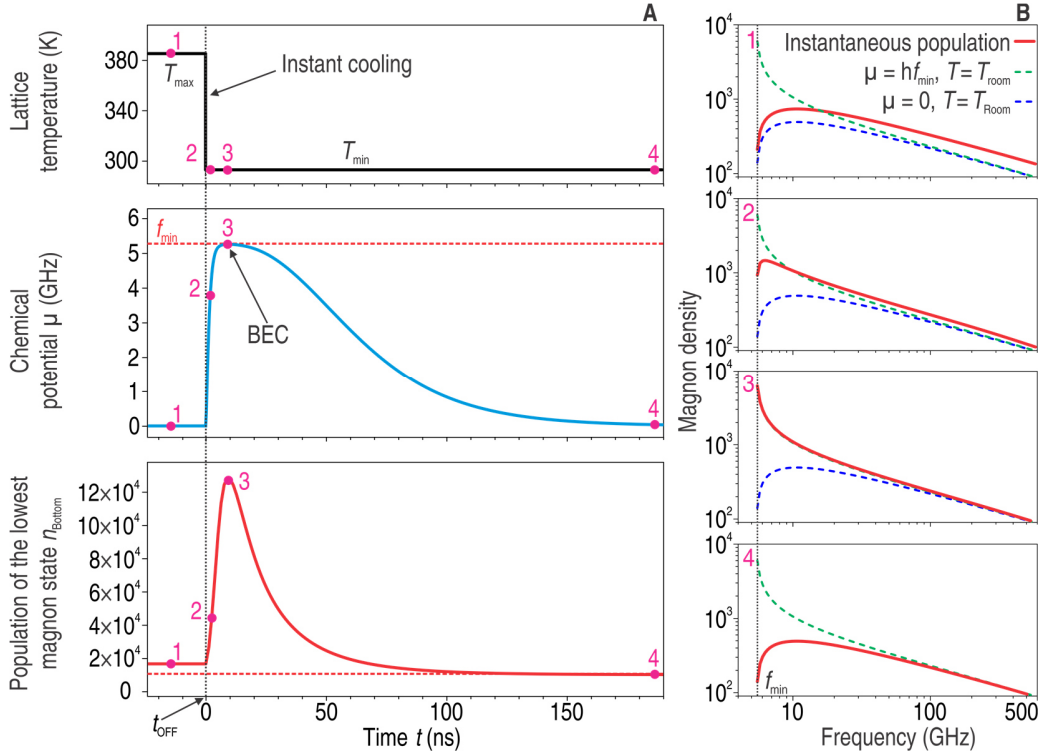


Figure S2. A) Time evolution of the temperature of the phonon system (top panel), the magnon chemical potential (middle panel) and the magnon population at the lowest energy state (bottom panel). The moment in time of the instant cooling is marked by t_{OFF} and the vertical dashed line. B) Frequency distributions of the quasi-particles density for different times. The red lines in panels (1-4) show the snapshots of the magnon densities (for the times marked by the pink dots in Fig. S2A calculated using the dynamics equations. Dashed blue lines show the steady-state room-temperature distribution calculated using Eq. (1) in the manuscript. The green dashed lines denote the distribution when the chemical potential μ is equal to the minimal magnon energy hf_{\min} . Panel 1: Stationary heated case before the instant cooling. Panel 2: Distribution just after the instant cooling. Panel 3: Snapshot of magnon density when the chemical potential μ reaches the minimal energy hf_{\min} , resulting in BEC. Panel 4: Final room temperature equilibrium state.

2. Fabrication of the YIG/Pt nano-structures under investigation

The investigated YIG/Pt strips are 500 nm (Fig.1, Fig. 2A-B and Fig. 3) and 1000 nm (Fig. 2C-E) wide and 5 μm long. The distance between the leads is 4 μm . The structures were fabricated using a YIG film of 70 nm thickness grown by means of Liquid Phase Epitaxy (LPE) on a (111) oriented Gadolinium Gallium Garnet (GGG) substrate (13). Standard microwave-based ferromagnetic resonance (FMR) measurements yield a Gilbert damping parameter of $\alpha_{\text{YIG}} = 1.8 \times 10^{-4}$ for the bare out-of-plane magnetized YIG film with an inhomogeneous broadening of $\mu_0 H_0 = 0.1$ mT, and an effective saturation magnetization of $M_s = 123$ kA/m. Next, plasma-assisted cleaning was used to remove potential contaminations before the sample was transferred into a Molecular Beam Epitaxy (MBE) facility, where the sample was heated up to 200°C for 2 hours at a pressure of $p = 3.7 \times 10^{-9}$ mbar before a 7 nm thick Pt layer was deposited on top of the YIG film⁴. The deposited Pt layer was found to increase the Gilbert damping to $\alpha_{\text{YIG/Pt}} = 1.2 \times 10^{-3}$. The subsequent structuring of the YIG/Pt strips was achieved by Electron-Beam Lithography and Argon-Ion Milling⁵ to a depth of approximately 40 nm. Afterwards the 150 nm thick gold contacts were structured by Electron-Beam Lithography and Electron-Beam evaporation, with a 10 nm thick Titanium seed layer. Then a focused Ion-Beam was used to remove the YIG adjacent to the structures and to polish the edges, resulting in a material removal to a depth of 300 nm. The resistance of the investigated devices is typically in the range of 600 Ohm for a width of 500 nm and in the range of 400 Ohm for a width of 1000 nm.

3. Spin-wave dispersion in the YIG nano-structures

The dispersion relations were obtained by means of micromagnetic simulations which were performed using MuMax3⁶ and from analytic theory – see Fig. S3.

The following parameters were used for the micromagnetic simulations. The size of the waveguide is 20 $\mu\text{m} \times 500$ nm \times 70 nm (length \times width \times thickness). The mesh was set to 10 nm \times 10 nm \times 70 nm. The following parameters for YIG were used: Saturation magnetization $M_s = 123$ kA/m, exchange constant $A = 3.5$ pJ/m, and Gilbert damping $\alpha = 2 \times 10^{-4}$. In the simulations, the damping at the ends of the waveguides was set to increase exponentially to 0.5 in order to eliminate spin-wave reflections. The external field is 188 mT for both, the Backward Volume and the Damon Eshbach geometry (11). In order to excite spin-wave dynamics in the waveguide, a sinc field pulse was applied to a 50 nm wide area in the center of the waveguide.

⁴ M. B. Jungfleisch, V. Lauer, R. Neb, A. V. Chumak, B. Hillebrands, Improvement of the yttrium iron garnet/platinum interface for spin pumping-based applications. *Appl. Phys. Lett.* **103**, 022411 (2013).

⁵ P. Pirro, T. Brächer, A. V. Chumak, B. Lägel, C. Dubs, O. Surzhenko, P. Görnert, B. Leven, B. Hillebrands, Spin-wave excitation and propagation in microstructured waveguides of yttrium iron garnet/Pt bilayers. *Appl. Phys. Lett.* **104**, 012402 (2014).

⁶ A. Vansteenkiste, J. Leliaert, M. Dvornik, M. Helsen, F. Garcia-Sanchez, B. Van Waeyenberge, The design and verification of MuMax3, *AIP Adv.* **4**, 107133 (2014).

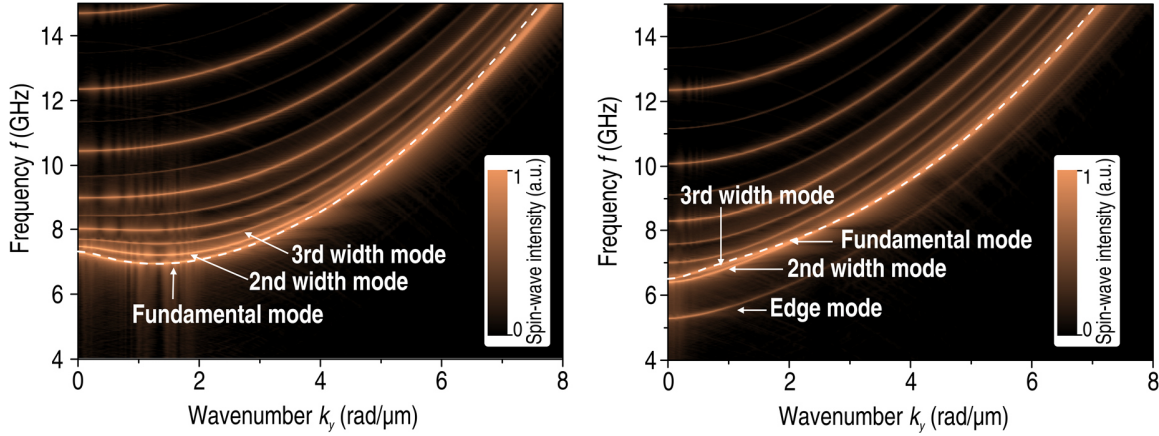


Figure S3. A) Simulated spin-wave intensity as a function of the frequency f and the wavenumber k_x along the waveguide for $\mathbf{B} \parallel \mathbf{x}$. B) Simulated spin-wave intensity as a function of the frequency f and the wavenumber k_x along the waveguide for $\mathbf{B} \parallel \mathbf{y}$. Dashed lines in both panels are dispersion curves calculated analytically for the first width mode.

To gain access to both, odd and even spin-wave-width modes, this area was slightly shifted away from the center along the short axis of the waveguide. The sinc field is given by $\mathbf{b}_z = b_0 \text{sinc}(2\pi f_c t)$, with an oscillation field $b_0 = 1 \text{ mT}$ and a cutoff frequency $f_c = 20 \text{ GHz}$. The out-of-plane component $M_z(x, y, t)$ of each cell was collected over a period of $t = 50 \text{ ns}$ and stored in $t_s = 12.5 \text{ ps}$ intervals, which results in a frequency resolution of $\Delta f = 1/t = 0.02 \text{ GHz}$, whereas the highest resolvable frequency was $f_{\max} = 1/(2t_s) = 40 \text{ GHz}$. The fluctuations in $m_z(x, y, t)$ were calculated for all cells via $m_z(x, y, t) = M_z(x, y, t) - M_z(x, y, t=0)$, where $M_z(x, y, t=0)$ corresponds to the ground state. To obtain the spin wave dispersion curves, a two-dimensional fast Fourier transformation in space and time has been performed⁷.

To visualize the dispersion curve, Fig. S3 shows a 3D colour map of the spin-wave intensity, which is proportional to $m_z^2(k_x, f)$, in logarithmic scale as a function of f and k_x . In both configurations, several width modes are visible, of which the first three are marked in the graphs in Fig. S3. Since the first three width modes are at similar frequencies, they cannot be distinguished in the experiment. The energy minimum, where the generation of the Bose Einstein condensate is expected, is in both cases within the wave-vector range accessible with Brillouin-Light Scattering (BLS) spectroscopy ($k_x = 1.3 \text{ rad}/\mu\text{m}$ for $\mathbf{B} \parallel \mathbf{y}$ and $k_x = 0 \text{ rad}/\mu\text{m}$ for $\mathbf{B} \parallel \mathbf{x}$). The frequency of the minimum of the magnon spectrum coincides with the ferromagnetic resonance frequency ($k=0$) in the case of the Damon Eshbach $\mathbf{B} \parallel \mathbf{x}$ geometry and differs by a value of 380 MHz in the case of the Backward Volume geometry $\mathbf{B} \parallel \mathbf{y}$ (this difference is on the order of magnitude of the frequency resolution of the BLS spectroscopy). In general, the calculated frequency at the bottom of the magnon spectrum agrees well with the frequency of the BEC peak observed in the experiment taking into account the decrease of the saturation magnetization due to the increase in temperature within the YIG nano-structure. Higher thickness modes are not visible in the simulations, since only one cell over the thickness is taken into account.

⁷ G. Venkat, D. Kumar, M. Franchin, O. Dmytriiev, M. Mruczkiewicz, H. Fangohr, A. Barman, M. Krawczyk, A. Prabhakar, Proposal of a standard micromagnetic problem: Spin wave dispersion in a magnonic waveguide, *IEEE Trans. Magn.* 49, 524 – 529 (2013).

The analytic results, shown as dashed white lines in Fig. S3 were calculated using Kalinikos and Slavin's theory for spin waves in thin films⁸ taking into account higher waveguide modes⁹. For the analytical calculations, the same parameters were used as in the micromagnetic simulations. The effective field $B_{\text{ext}} = 174.5$ mT in the Damon Eshbach geometry, which is slightly smaller than the applied external field due to the demagnetizing field, was extracted from the simulation.

4. Measurements of the magnon density by time-resolved Brillouin Light Scattering (BLS) spectroscopy

In order to apply current pulses to the Pt nano-strip, a pulse generator (*Keysight 81160 A*) providing transition times down to 1 ns is connected to the sample using RF probes (*picoprobes*). For the BLS measurements (14), a laser beam with a wavelength of 457 nm and a power of 1.5 mW is focused through the transparent substrate onto the center of the structures. The laser-spot size is approximately 400 nm in diameter. The experiment was performed with a repetition rate of 1 μ s. The intensity of the frequency-shifted and backscattered light is proportional to the spin-wave intensity (14). The maximal spin-wave wave-vector, which can be detected is given by the laser wavelength and the numerical aperture of the objective $N_A = 0.85$. In our setup, spin waves with an in-plane wave vector up to 23.4 rad/ μ m can be detected. The frequency shifted light passes a three-pass Tandem-Fabry Perot interferometer and is detected frequency selectively by a single photon counting module with a resolution of $\Delta f_{\text{BLS}} = 150$ MHz. The output of the detector is connected to a fast data acquisition module, which is synchronized with the applied pulses. The time resolution is limited by the time the scattered photons stay in the interferometer, which is determined by the finesse of the interferometer and the distance between the mirrors ($d = 5$ mm in the experiment), resulting in a time resolution of approximately $\Delta t = 2$ ns. An in-plane biasing field of $B_{\text{ext}} = 188$ mT is applied, which is sufficiently large to magnetize the strips in the direction of the applied field. The orientation of the external field with respect to the strip is changed by turning the sample by 90 degrees.

5. Simulations of the temporal evolution of YIG/Pt nano-structure by COMSOL Multiphysics Software

The numerically calculated time evolution of the temperature of the YIG/Pt strips was determined by solving a 3D heat-transfer model of the experimental set-up with the COMSOL Multiphysics Software using the heat transfer module and the electric currents module.

⁸ B. A. Kalinikos, A. N. Slavin, Theory of dipole-exchange spin wave spectrum for ferromagnetic films with mixed exchange boundary conditions, *J. Phys. C: Solid State Phys.* **19**, 7013-7033 (1986).

⁹ T. Brächer, O. Boulle, G. Gaudin, P. Pirro, Creation of unidirectional spin-wave emitters by utilizing interfacial Dzyaloshinskii-Moriya interaction. *Phys. Rev. B* **95**, 064429 (2017).

Parameter	Material	Value/ Source
Density	YIG	5170 kg m^{-3} A. E. Clark, R. E. Strakna, Elastic constants of single-crystal YIG, <i>J. Appl. Phys.</i> 32 , 1172 (1961)
Heat conductivity	YIG	$6 \text{ W m}^{-1}\text{K}^{-1}$ A. M. Hofmeister, Thermal diffusivity of garnets at high temperature, <i>Phys. Chem. Minerals</i> 33 , 45-62 (2006)
Heat capacity	YIG	$570 \text{ J kg}^{-1} \text{ K}^{-1}$ M. Guillot, F. Tchéou, A. Marchand, P. Feldmann, R. Lagnier, Specific heat in Erbium and Yttrium Iron garnet crystals, <i>Z. Phys. B – Condensed Matter</i> 44 , 53-57 (1981)
Density	GGG	7080 kg m^{-3} A. M. Hofmeister, Thermal diffusivity of garnets at high temperature, <i>Phys. Chem. Minerals</i> 33 , 45-62 (2006)
Heat conductivity	GGG	$7.94 \text{ W m}^{-1}\text{K}^{-1}$ A. M. Hofmeister, Thermal diffusivity of garnets at high temperature, <i>Phys. Chem. Minerals</i> 33 , 45-62 (2006)
Heat capacity	GGG	$400 \text{ J kg}^{-1} \text{ K}^{-1}$ A. M. Hofmeister, Thermal diffusivity of garnets at high temperature, <i>Phys. Chem. Minerals</i> 33 , 45-62 (2006)
Density	Pt	21450 kg m^{-3} D. Lide, CRC Handbook of Chemistry and Physics, 89th ed. (Taylor & Francis, London, 2008)
Electrical conductivity	Pt	$1.41 \times 10^6 \text{ S m}^{-1}$ Measured
Resistance-Temperature Coefficient	Pt	$7.135 \times 10^{-4} \text{ K}^{-1}$ Measured
Thermal Conductivity	Pt	$22 \text{ W m}^{-1} \text{ K}^{-1}$ S. Yoneoka, J. Lee, M. Liger, G. Yama, T. Kodama, M. Gunji, J. Provine, R. T. Howe, K. E. Goodson, T. W. Kenny, Electrical and thermal conduction in atomic layer deposition nanobridges down to 7 nm thickness, <i>Nano Lett.</i> 12 , 683-686 (2012)
Heat capacity	Pt	$130 \text{ J kg}^{-1} \text{ K}^{-1}$ G. T. Furukawa, M. L. Reilly, J. S. Gallagher, Critical Analysis of Heat Capacity data and evaluation of thermodynamic properties of Ruthenium, Rhodium, Palladium, Iridium, and Platinum from 0 to 300K. A survey of the literature data on Osmium, <i>J. Phys. Chem. Ref. Data</i> 3 , 163 (1974)
Density	Au	1900 kg m^{-3} COMSOL Library

Parameter	Material	Value/ Source
Electrical conductivity	Au	$4.1 \times 10^7 \text{ S m}^{-1}$ COMSOL Library
Thermal Conductivity	Au	$190 \text{ W m}^{-1} \text{ K}^{-1}$ G. Langer, J. Hartmann, M. Reichling, Thermal conductivity of thin metallic films measured by photothermal profile analysis, <i>Rev. Sci. Instrum.</i> 68 , 3 (1997)
Heat capacity	Au	$130 \text{ J kg}^{-1} \text{ K}^{-1}$ T. H. Geballe, W. F. Giauque, The heat capacity and entropy of Gold from 15 to 300°K, <i>J. Am. Chem. Soc.</i> 1952 , 74)
Density	Ti	4500 kg m^{-3} COMSOL Library
Electrical conductivity	Ti	$2 \times 10^6 \text{ S m}^{-1}$ COMSOL Library
Thermal Conductivity	Ti	$22 \text{ W m}^{-1} \text{ K}^{-1}$ C. Y. Ho, R. W. Powell, P. E. Liley, Thermal conductivity of the elements, <i>J. Phys. Chem. Ref. Data</i> 1 , 2 (1972)
Heat capacity	Ti	$521.4 \text{ J kg}^{-1} \text{ K}^{-1}$ C. W. Kothen, H. L. Johnston, Low Temperature Heat Capacities of Inorganic Solids. XVII. Heat Capacity of Titanium from 15 to 305°K. <i>J. Am. Chem. Soc.</i> 75 , 3101 (1953)
Heat capacity	Air	$1047.6366 - 0.3726 T + 9.4530 \times 10^{-4} T^2 - 6.0241 \times 10^{-7} T^3 + 1.2859 \times 10^{-10} T^4 \text{ J kg}^{-1} \text{ K}^{-1}$ COMSOL Library
Thermal Conductivity	Air	$-0.0023 + 1.1548 \times 10^{-4} T - 7.9025 \times 10^{-8} T^2 + 4.1170 \times 10^{-11} T^3 - 7.4386 \times 10^{-15} T^4 \text{ W m}^{-1} \text{ K}^{-1}$ COMSOL Library
Density	Air	$8.53 T^{-1} \text{ kg m}^{-3}$ COMSOL Library

Table S4. Parameters used for the COMSOL simulations of the temperature evolution in YIG/Pt nano-structure.

Hereby, the conventional heat conduction differential equation and the differential equations for current conservation are solved taking into consideration the boundary conditions applied to the model as well as the material parameters of the materials used. The model comprises a $9 \mu\text{m} \times 4.5 \mu\text{m} \times 6.5 \mu\text{m}$ large volume which includes half of the strip, exploiting the symmetry of the system with respect to its long axis. The simulated geometry

includes the YIG/Pt strip, a part of the Au leads, which have a width of 1000 nm where they meet the strip and a width of 8 μm at a distance of 1 μm to the strip. In addition, the removal of the material by focused Ion-Beam with a width of 4 μm at the sides of the strip with a depth of 300 nm is taken into account. The used material parameters can be found in Table S4. The electrical conductivity and the corresponding temperature coefficient of Pt were measured experimentally, whereas the other parameters are taken from the referenced literature or from the COMSOL library. For the heat-transfer model, the boundary on the edges were set to the symmetry boundary condition for the according edges and to open boundary for the others. For the electric-currents model they were set to electric insulation, except for the two faces of the leads where the electric potential is applied. The Joule heating is modelled for all metallic layers in the system. The simulation differs from the experiment by the fact that the convective cooling due to the surrounding air as well as the laser heating are not implemented.

Figure S5 shows the obtained temperature profile in the center of the Pt overlayer. The profile was obtained for a 300 ns long pulse with an amplitude of $U_{\text{Sim}} = 1.872 \text{ V}$ (corresponding to a set voltage of $U = 1.05 \text{ V}$ at the pulse generator for a 50 Ohms load resistance in the experiment) and transition times of 1 ns at the edges. It can be seen that the temperature increases rapidly just after the current pulse is applied to Pt but tends to saturate. After a time of approximately 300 ns the temperature still grows but the heating has already strongly decelerated allowing for the formation of the quasi-equilibrium between the magnon and phonon temperatures¹⁰ considered in the theoretical model. The maximal temperature reached at the end of the applied current pulse in this particular case is 491 K. This value was confirmed by an additional continuous-regime experiment in which the resistance of the Pt overlayer was used directly as a thermometer and was calibrated using a thermo-couple detector. The continuous current corresponding to the same voltage $U = 1.05 \text{ V}$ resulted in a steady state temperature of the Pt overlayer of 550 K. The temperature of the YIG is assumed to be smaller and, since the experiment was performed in the pulsed regime, it consequently never reaches the Curie temperature of YIG of about 550 K (15).

As it is seen in Fig. S5A, switching off the current pulse results in a fast decrease in temperature of the YIG/Pt nano-structure due to the thermal diffusion in the quasi-bulk surroundings. The cooling rate is not constant and decreases with time. Moreover, our simulations further revealed (not shown) that the cooling rate depends on the duration of the applied current pulse which is associated with the increase in temperature of the surroundings of the nano-structure for long current pulses.

To prove the crucial role of the fast cooling for the BEC, additional measurements were performed where the current pulses were switched off with fall times of 50 ns and 100 ns – see Fig. 2 in the main text of the manuscript. It is evident that the condensate disappears for long fall times, i.e. slow cooling rates. For reference, Fig. S5B shows the corresponding simulated temperature evolutions in the phonon system. The maximal cooling rates indicated in Fig. S5B clearly show that a cooling rate of 2 K/ns is already too slow to trigger the magnon BEC, while a rate of 20.5 K/ns is still fast enough.

¹⁰ M. Agrawal, V. I. Vasyuchka, A. A. Serga, A. D. Karenowska, G. A. Melkov, and B. Hillebrands, Direct measurement of magnon temperature: New insight into magnon-phonon coupling in magnetic insulators. *Phys. Rev. Lett.* **111**, 107204 (2013).

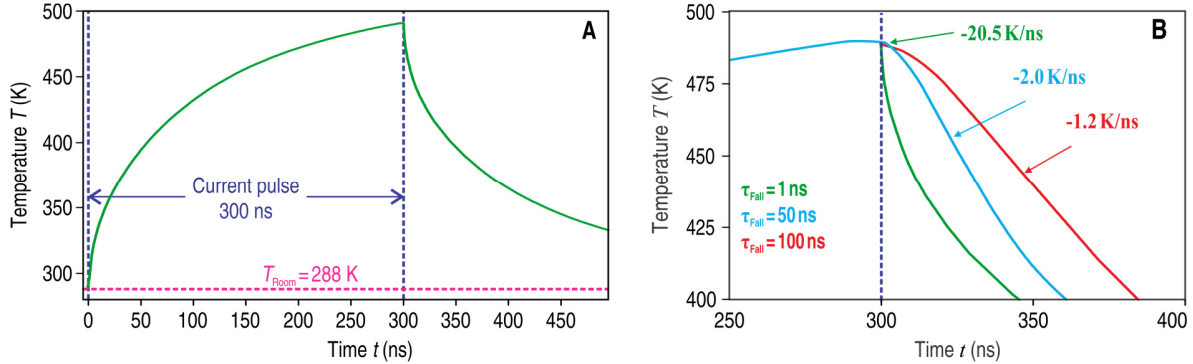


Figure S5. A) Simulated temperature as a function of time in the middle of the Pt overlayer for a 300 ns long pulse with a voltage of 1.05 V applied to a 1 μm wide waveguide. The fall time of the pulse was 1 ns. The dashed blue lines indicate the time when the pulse is present. The room temperature is marked with the dashed pink line. B) Simulated temperature as a function of time for different fall times $\tau_{\text{Fall}} = 1$ ns (green line), $\tau_{\text{Fall}} = 50$ ns (blue line), $\tau_{\text{Fall}} = 100$ ns (red line). The maximal time derivatives are marked at their respective time of occurrence.

6. Dependence of the BEC on the parameters of the experiment and on the direction of the applied magnetic field

The described formation of the magnon BEC is driven by the change of the temperature of the phonon system. In order to prove this, a set of measurements using different structure sizes of width of 500 nm and 1000 nm, of different scanning laser powers in the range from 0.75 mW to 3.3 mW, different magnetic fields in the range from 84 mT to 270 mT, and different scanning points on the structure were performed. The experimental finding of the BEC formation, which manifests itself as a strong magnon peak at the bottom of the spectrum, could always be confirmed.

Furthermore, the fact that there is no dependence of the phenomenon on the direction of the external field was confirmed by changing the direction of the applied field. Figure S6 shows the corresponding time resolved BLS spectra in the case that the external field is applied perpendicular (Panel A, $\mathbf{B} \parallel \mathbf{y}$) or parallel (Panel C, $\mathbf{B} \parallel \mathbf{y}$) to the long axis of the strip for similar pulse durations of $\tau_P = 120$ ns and $\tau_P = 150$ ns. Further, the integrated intensity of the fundamental mode is shown for both cases in panel B ($\mathbf{B} \parallel \mathbf{y}$) and panel D ($\mathbf{B} \parallel \mathbf{x}$), which was in accordance with the results of the micromagnetic simulations (see Fig. S3). The frequencies of the fundamental modes are slightly larger if the magnetic field is applied parallel to the long axis of the strip. This is associated with the demagnetization fields that result in a smaller internal field when the strip is magnetized along its short axis. In addition, the inhomogeneity of the demagnetization fields leads to the formation of an edge mode with a frequency below the fundamental mode of the strip. The edge mode is also visible in the experiment (see. Fig. S6 B).

The formation of the magnon BEC is observed in both cases at the bottom of the band of the waveguide modes, i.e., the lowest frequency of the fundamental mode. Even though the edge mode is the total energy minimum at room temperature equilibrium, it cannot be separated in the

experiment from the fundamental mode during the BEC formation since, in contrast to the other modes, its frequency is not significantly decreased during the pulse. The reason for this is that the frequency of the edge mode strongly depends on the strength of the demagnetization fields. These fields are reduced as well when the saturation magnetization is decreased due to Joule heating. This behaviour was confirmed by additional MuMax3 simulations (not shown). The formation of the BEC for both field directions excludes a contribution from the Spin-Hall effect to the observed condensation, since it would only lead to an efficient injection of spin current when the magnetization is perpendicular to the direction of the electric current (18). Moreover, since the phenomenon does neither depend on the direction nor on the value of the applied magnetic field (and thus also not on the frequency of the BEC), we can conclude that the Oersted fields generated by the electric current in the Pt overlayer do not play any sizable role in the experiments.

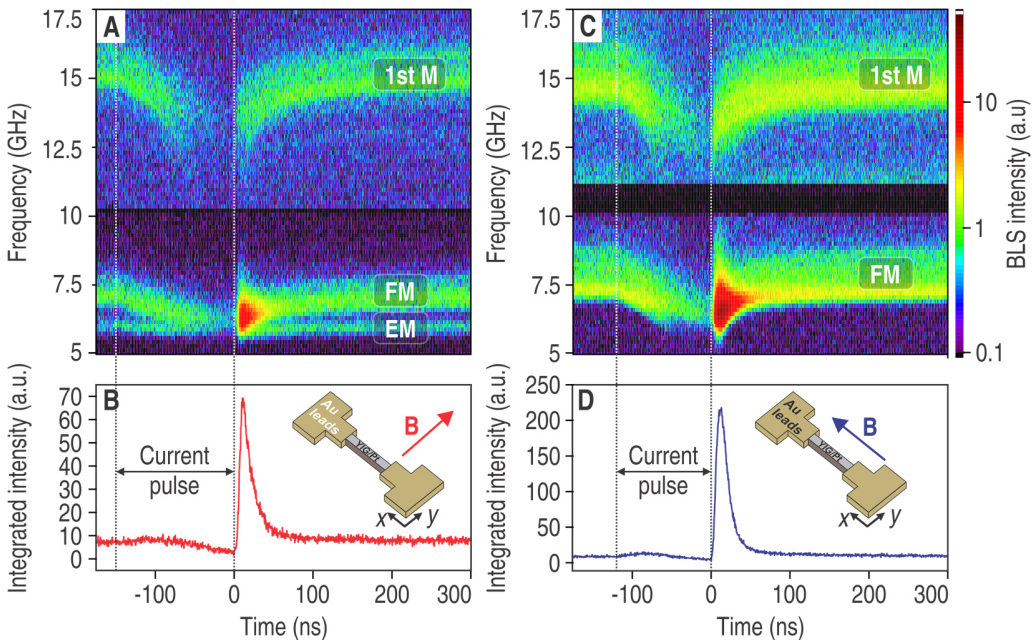


Figure S6. A) BLS spectrum as a function of time. The BLS signal (color-coded, log scale) is proportional to the density of magnons. FM indicates the fundamental mode, EM the edge mode, and 1st M the first thickness mode. The vertical dashed lines indicate the start and the end of the pulse ($\tau_P = 150$ ns, $U = 0.9$ V). The external field was parallel to the short axis of the strip ($\mathbf{B} \parallel \mathbf{y}$). B) BLS spectrum as a function of time for the case when the external magnetic field is parallel to short axis of the strip ($\mathbf{B} \parallel \mathbf{x}$), ($\tau_P = 120$ ns, $U = 0.9$ V). C,D) Normalized magnon intensity integrated from 4.95 GHz to 8.1 GHz as a function of time for the cases in A) and B). The insets show the sample and measurement geometry.

7. Dependence of the BEC threshold on the current pulse duration

The threshold voltages are determined experimentally for different pulse durations $18 \text{ ns} \leq \tau_p \leq 175 \text{ ns}$. For each pulse duration, BLS measurements were performed for different voltages. The maximum of the intensity integrated over the frequency range of the fundamental mode was extracted and plotted as a function the applied voltage for each pulse duration. This yields graphs similar to the depiction in Fig. 3B in the main manuscript. The corresponding threshold voltage is determined by fitting the slope linearly and calculating the intercept with the averaged subcritical (thermal) BLS intensity. The extracted threshold voltages are shown in Fig. S7. As can be seen, the threshold voltage increases for the shortest pulse durations, whereas it saturates for the longest ones. This is due to the finite timescale of the Joule heating, which is in agreement with our model. The threshold temperature (i.e., the critical magnon density) should be independent of the applied voltage. As expected, the COMSOL simulations yielded similar values for the threshold temperature for all $\tau_p > 70 \text{ ns}$ (blue points in Fig. S7). The increased threshold temperature for the shorter pulses was likely mediated by the finite interaction time between the phonon system and the magnon system which is given by the frequency dependent lifetime of the magnons $t_m < 21 \pm 4 \text{ ns}$. This results in the fact that the temperature of the magnon system¹⁰ does not reach the phonon temperature at the end of the pulse and is therefore smaller. Nevertheless, as it is supported by the experimental findings, the absence of the quasi-equilibrium between magnon and phonon systems before the fast cooling starts does not impede the phenomena of the BEC of magnons as long as the critical magnon density is reached.

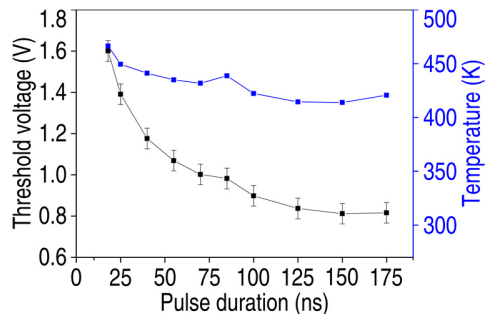


Figure S7. Threshold voltage as a function of the pulse duration (black squares) and corresponding simulated temperatures at the end of the pulses (blue squares).